



EUROfusion

EUROFUSION WP15ER-PR(15) 14275

JA Morales et al.

Edge Localized Mode Rotation and the Nonlinear Dynamics of Filaments

Preprint of Paper to be submitted for publication in
Physics of Plasmas



This work has been carried out within the framework of the EUROfusion Consortium and has received funding from the Euratom research and training programme 2014-2018 under grant agreement No 633053. The views and opinions expressed herein do not necessarily reflect those of the European Commission.

This document is intended for publication in the open literature. It is made available on the clear understanding that it may not be further circulated and extracts or references may not be published prior to publication of the original when applicable, or without the consent of the Publications Officer, EUROfusion Programme Management Unit, Culham Science Centre, Abingdon, Oxon, OX14 3DB, UK or e-mail Publications.Officer@euro-fusion.org

Enquiries about Copyright and reproduction should be addressed to the Publications Officer, EUROfusion Programme Management Unit, Culham Science Centre, Abingdon, Oxon, OX14 3DB, UK or e-mail Publications.Officer@euro-fusion.org

The contents of this preprint and all other EUROfusion Preprints, Reports and Conference Papers are available to view online free at <http://www.euro-fusionscipub.org>. This site has full search facilities and e-mail alert options. In the JET specific papers the diagrams contained within the PDFs on this site are hyperlinked

1 **Edge Localized Mode Rotation and the Nonlinear Dynamics of**
2 **Filaments**

3 J.A. Morales,* M. Bécoulet, X. Garbet, G. Dif-Pradalier,
4 A. Fil, E. Nardon, C. Passeron, and G. Latu
5 *CEA, IRFM, 13108 Saint-Paul-Lez-Durance, France*

6 F. Orain and M. Hoelzl
7 *Max Planck Institute for Plasma Physics,*
8 *Boltzmannstr. 2, 85748 Garching, Germany*

9 S. Pamela
10 *EUROfusion Consortium, JET, Culham Science Centre,*
11 *Abingdon OX14 3DB, United Kingdom*

12 P. Cahyna
13 *Institute of Plasma Physics ASCR, 182 00 Prague 8, Czech Republic*

14 G.T.A. Huijsmans
15 *ITER Organization, Route de Vinon sur Verdon,*
16 *13115 Saint Paul Lez Durance, France*

17 (Dated: July 13, 2015)

Abstract

18

19 The existence of Edge Localised Modes (ELM) rotating precursors few milliseconds before an
20 ELM crash was reported in many experiments (KSTAR, MAST, AUG, NSTX, TCV, JET). More-
21 over, in these experiments, similar nonlinear dynamics are observed at the ELM crash. In the
22 present letter, the rotation of ELM precursors and the dynamics of expelled filaments at the ELM
23 crash are explained using both, linear ballooning theory and nonlinear MHD simulations with the
24 JOREK code. It is shown that unstable ballooning modes, localised at the pedestal, grow and ro-
25 tate mainly in the electron diamagnetic direction in the laboratory reference frame. Approaching
26 the ELM crash, this regular rotation decreases corresponding to the moment when the magnetic
27 reconnections and edge ergodisation occur. During the highly nonlinear ELM crash, the ELM
28 filaments are cut from the main plasma due to the strong sheared mean flow that is nonlinearly
29 generated via the Maxwell stress tensor.

* Email: jorge.a.morales@outlook.com

30 I. INTRODUCTION

31 Edge Localised Modes are MHD instabilities that appear at the edge of the tokamak
32 plasma in high confinement mode (H-mode). They are characterised by periodic bursts of
33 matter and energy. The crash of this instability leads to the relaxation of the edge pressure
34 pedestal. Then the edge pedestal rebuilds and another ELM cycle occurs. The quantity
35 of energy that is expelled periodically can cause partial erosion or melting of plasma-facing
36 components (PFC). This could limit the operational capabilities of future larger tokamak
37 devices like ITER and DEMO. For recent review articles on ELMs we refer to [1, 2].

38 In recent years, measurements performed with electron cyclotron emission imaging
39 (ECEI) have provided insights on the dynamics of this instability prior to and during
40 an ELM crash. ECEI measurements in the KSTAR tokamak [3] show that the ELM evolu-
41 tion can be separated in three different phases. The first is a linear phase where the localised
42 mode grows, the second is a quasi-quiescent state where the mode growth decreases and the
43 third is when the ELM crash occurs. In the majority of cases, during the linear phase, the
44 rotation of the precursors (structures preceding an ELM crash) is observed in the electron
45 diamagnetic direction. Near the crash, the rotation speed of the precursors decreases and
46 the precursor structure seems to extend radially towards the last closed flux surface where
47 the ELM crash occurs. These measurements are in agreement with AUG ECEI measure-
48 ments [4, 5]. In AUG, the rotation of the ELM precursors is also found in the electron
49 diamagnetic direction but the first-expelled ELM filament is observed to reverse rotation
50 and to propagate in the ion diamagnetic direction. In a third device, NSTX, gas puffing
51 imaging is used to characterise the precursors rotation and the filament expulsion of an ELM
52 [6]. In this last device the precursors are also observed rotating in the electron diamagnetic
53 direction and at the crash, the filament slow down and also reverses rotation direction
54 (propagating in the ion diamagnetic direction). In TCV with magnetic measurements [7]
55 and in MAST using beam emission spectroscopy [8] similar results were obtained. Recently
56 in JET, fast infra-red thermography measurements at the divertor [9] show ELM precursors
57 stripes moving radially outward. This also suggests ELM precursors structures rotating in
58 the electron diamagnetic direction.

59 Several instabilities can be candidate to explain the ELM precursors. The microtearing
60 mode instability has been proposed as one of the possible candidates [8, 10]. This instability

61 shares several characteristics with the experimental measurements but its radial extend is
62 short (of the order of the ion Larmor radius). This last feature is incompatible with some
63 of the observations. Also peeling modes and drift waves can be considered but, the firsts
64 are characterised by low toroidal mode numbers that are inconsistent with the observa-
65 tions and the seconds are electrostatic in nature, a characteristic not compatible with the
66 electromagnetic properties of ELM precursors.

67 Ballooning modes are strong candidates to explain the observations [11]. In this
68 manuscript we will focus on this last instability. Analytically in the linear phase we consider
69 ideal and resistive ballooning modes taking into account bi-fluid diamagnetic effects. Nu-
70 merical calculations using the nonlinear code JOEAK [12, 13] are performed. A comparison
71 with the analytical results in the linear stage is carried out. This numerical code is also used
72 to analyse the nonlinear saturation of the instability and to characterise the mechanism that
73 allows to explain the reversal of the filaments rotation at the ELM crash.

74 II. THE LINEAR BALLOONING MODE ROTATION

75 The reduced MHD equations over the magnetic flux Ψ , the electric potential Φ and
76 the pressure P , are used to calculate the dispersion relation associated with the balloon-
77 ing instability. We use the gyro-viscous cancellation to simplify the equation over Φ (see
78 e.g. [14]). The ballooning representation is used to reduce the two-dimensional problem to
79 one dimension (see e.g. [15]). The following ansatz is applied

$$80 \quad \Phi(\phi, \theta, t) = \sum_{l=-\infty}^{+\infty} \widehat{\Phi}(\theta + 2\pi l) e^{i(n[\phi - q(\theta + 2\pi l)] - \omega t)}, \quad (1)$$

81 for a ballooning mode $l = 0$. Also, for simplification, we consider the reference frame rotating
82 with the $\mathbf{E} \times \mathbf{B}$ velocity, hence in this reference frame $V_{\mathbf{E} \times \mathbf{B}} = 0$ ($\widehat{\Phi}_{n=0} = 0$). We will add
83 the $\mathbf{E} \times \mathbf{B}$ velocity contribution at the end of the linear calculation.

84 Using these hypothesis the following dispersion relation, in dimensionless form, is found

$$\omega(\omega - \omega_i^*) \left[(\omega - \omega_e^*) + \frac{q^2 R_0^2 (\omega - \omega_e^* + i\eta k_\theta^2)^2}{i\eta k_\theta^2 s^2} [\omega(\omega - \omega_i^*) + 2\gamma_I^2] \right] +$$

$$\gamma_I^2 (\omega - \omega_e^*) \left(1 + \frac{(\omega - \omega_e^* + i\eta k_\theta^2) (2s(1-s) - 1)}{2i\eta k_\theta^2 s^2} \right) = \frac{-q^2 R_0^2 (\omega - \omega_e^* + i\eta k_\theta^2)^2}{i\eta k_\theta^2 s^2} \gamma_I^4, \quad (2)$$

85 with $\omega_i^* = -\omega_e^* = d_i \frac{\partial P_0}{\partial r} k_\theta \mathbf{e}_\theta$, $d_i = \frac{1}{\omega_{Ci} \tau_A} = \frac{m_i}{e R_0 \sqrt{\rho_0 \mu_0}}$ and $\gamma_I = \left\{ -\frac{4}{B_0 R_0} \frac{\partial P_0}{\partial r} \right\}^{1/2}$,

86 with θ the poloidal direction, k_θ the poloidal wavenumber, $\omega_{i/e}^*$ the diamagnetic frequencies
 87 (ion/electron, non-dimensionalised by the Alfvén time τ_A), d_i the diamagnetic parameter,
 88 γ_I the ideal interchange growth rate, P_0 the axisymmetric pressure, q the safety factor, s
 89 the magnetic shear and η the dimensionless inverse Lundquist number. Also B_0 , ρ_0 , R_0 , μ_0
 90 and e are respectively a reference magnetic field, density, length, the magnetic permeability
 91 and electric charge.

92 At high resistivity ($\eta \rightarrow \infty$) and strong magnetic shear ($s \gg 1$) Eq. (2) simplifies to

$$93 \quad \omega(\omega - \omega_i^*)(\omega - \omega_e^*) = (i\gamma_\eta)^3 \quad \text{with} \quad \gamma_\eta = \left[\frac{k_\theta^2 q^2}{s^2} R_0^2 \eta \gamma_I^4 \right]^{1/3}. \quad (3)$$

94 Considering the diamagnetic frequencies: $\omega_i^* = -\omega_e^* = \omega_*$, the roots of the polynomial can
 95 be found using Cardan's method. Taking into account the change of variable: $\omega = i\gamma$, this
 96 dispersion relation can be simplified to

$$97 \quad \gamma(\gamma^2 + \omega_*^2) = \gamma_\eta^3. \quad (4)$$

98 Two limits can be identified in Eq. (4), for $\gamma_\eta \gg \omega_*$ the solution $\gamma \approx \gamma_\eta$ and if $\gamma_\eta \ll \omega_*$ we
 99 have $\gamma \approx \gamma_\eta^3 / \omega_*^2$. In the general case three roots exist, one real and two complex conjugates
 100 [16]. The most unstable root is always the real, the value of ω is pure imaginary because
 101 $\omega = i\gamma$, hence at this limit the unstable mode does not rotate in the considered reference
 102 frame.

103 Also at the ideal limit, $\eta \rightarrow 0$, and small magnetic shear ($s \approx 1$) the dispersion relation
 104 Eq. (2) simplifies to the second order polynomial [17, 18]

$$105 \quad \omega^2 - \omega_i^* \omega + \gamma_I^2 = 0. \quad (5)$$

106 Two distinct roots exist

$$107 \quad \omega_\pm = \frac{\omega_i^* \pm \sqrt{\omega_i^{*2} - 4\gamma_I^2}}{2}. \quad (6)$$

108 The system is unstable if: $|\omega_i^*/2| < |\gamma_I|$. And the ideal rotation frequency of the mode is:
 109 $\omega_i^*/2$ [19, 20]. In this case the unstable mode rotates at half of the diamagnetic frequency
 110 in the ion diamagnetic direction in the considered reference frame.

111 Moreover the roots of the general dispersion relation, Eq. (2), can be computed numer-
 112 ically. We find that in realistic cases, i.e., at low resistivity ($\eta < 10^{-7}$) the most unstable

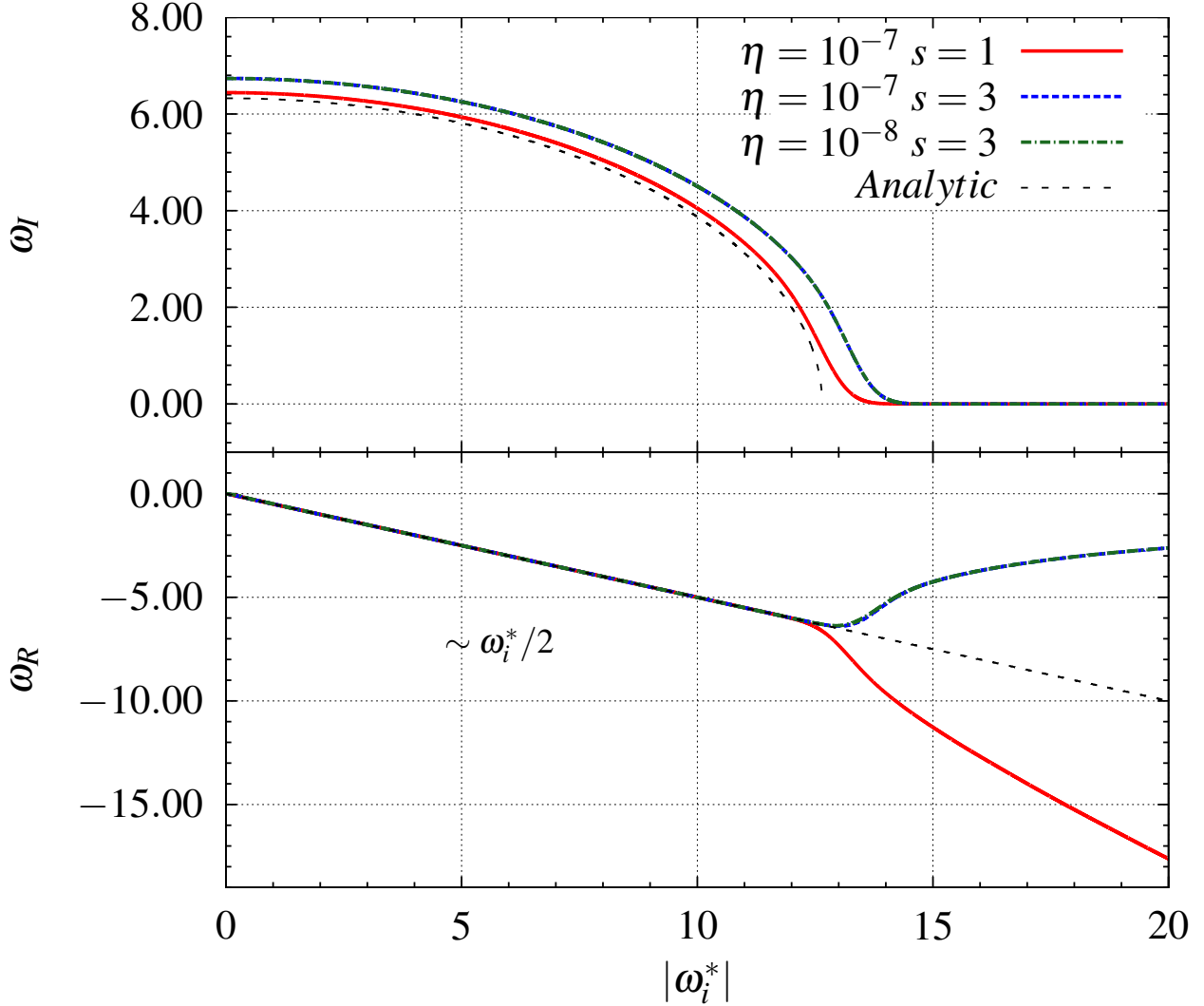


FIG. 1. Evolution of the roots with the diamagnetic frequency ω_i^* , (top) imaginary part (bottom) real part.

113 root is close to the ideal case Eq. (6). In Fig. 1 three computed cases are compared to the
 114 analytical solution Eq. (6). One can observe that the imaginary part of the root is close to
 115 the ideal theory if the magnetic shear is small. With increasing magnetic shear the calcu-
 116 lated mode is more unstable. On the other hand the real part of the root matches very well
 117 the analytical solution. The rotation of the mode, in the reference frame, is almost exactly
 118 $\omega_i^*/2$.

119 To calculate the mode poloidal rotation, in the laboratory reference frame, we add to
 120 the intrinsic ballooning mode rotation the poloidal $\mathbf{E} \times \mathbf{B}$ velocity and the parallel velocity
 121 $V_{\parallel} \cdot b_{\theta}$ (both velocities projected in the poloidal plane). The radial electric field in H-mode

122 is observed to be dominated at the pedestal by the radial pressure gradient of the main ions
 123 [21]. Also the pitch angle is considered to be small (\mathbf{B} is mainly in the toroidal direction).
 124 For these two reasons, in the pedestal region, the poloidal $\mathbf{E} \times \mathbf{B}$ velocity $V_{\mathbf{E} \times \mathbf{B}}$ can be
 125 approximated by

$$126 \quad V_{\mathbf{E} \times \mathbf{B}} \approx (\mathbf{E} \times \mathbf{B}) / B^2 \approx (\nabla_r P_i \times \mathbf{B}) / (enB^2). \quad (7)$$

Finally the poloidal rotation of the ballooning modes in the laboratory reference frame
 for the resistive and ideal limits writes

$$\text{Resistive: } V_{\text{mode}} = V_{\mathbf{E} \times \mathbf{B}} + V_{\parallel} \cdot b_{\theta} \quad (8)$$

$$\text{Ideal: } V_{\text{mode}} = V_{\mathbf{E} \times \mathbf{B}} + V_{\parallel} \cdot b_{\theta} + V_i^* / 2, \quad (9)$$

127 with the poloidal ion diamagnetic velocity $V_i^* \approx (\mathbf{B} \times \nabla P_i) / (enB^2)$. In dimensionless units
 128 (non-dimensionalised by the Alfvén speed) this velocity becomes

$$129 \quad V_i^* = \omega_i^* / k_{\theta} \approx d_i \nabla_r P. \quad (10)$$

130 Also the poloidal dimensionless $\mathbf{E} \times \mathbf{B}$ velocity at the pedestal, where the radial electric
 131 field is mostly induced by the radial pressure gradient, can be approximated by

$$132 \quad V_{\mathbf{E} \times \mathbf{B}} \approx -d_i \nabla_r P. \quad (11)$$

133 The radial gradient of the pressure is negative. Therefore, by convention, we have chosen the
 134 $\mathbf{E} \times \mathbf{B}$ and electron diamagnetic velocities in the positive direction and the ion diamagnetic
 135 velocity in the negative direction.

136 Using the JOREK code [12, 22, 23] the linear growth of the ballooning instability with
 137 and without diamagnetic effects can be analysed. ELM precursors were previously observed
 138 with the JOREK code without diamagnetic effects [22]. Here we include diamagnetic effects
 139 to analyse their effect on the precursors dynamics. The parameters used for the simulations
 140 are close to a JET tokamak plasma, as in Ref. [24]. Realistic values of the inverse Lundquist
 141 number, d_i parameter and normalised parallel heat conductivity are typically: $\eta = 10^{-8}$,
 142 $d_i = 10^{-2}$ and $\kappa_{\parallel} = 8000$ [25]. These values correspond to the following tokamak parameters
 143 in JET: $R_0 = 2.9 \text{ m}$, $B_0 = 1.8 \text{ T}$, $n_{ped} = 3.3 \cdot 10^{19} \text{ m}^{-3}$ and $T_{eped} = T_{iped} = 1.8 \text{ keV}$.

144 The magnetic flux perturbation is presented in Fig. 2. Without diamagnetic effects,
 145 $d_i = 0$, the mode grows and rotates at low speed, as was found in Ref. [12]. On the

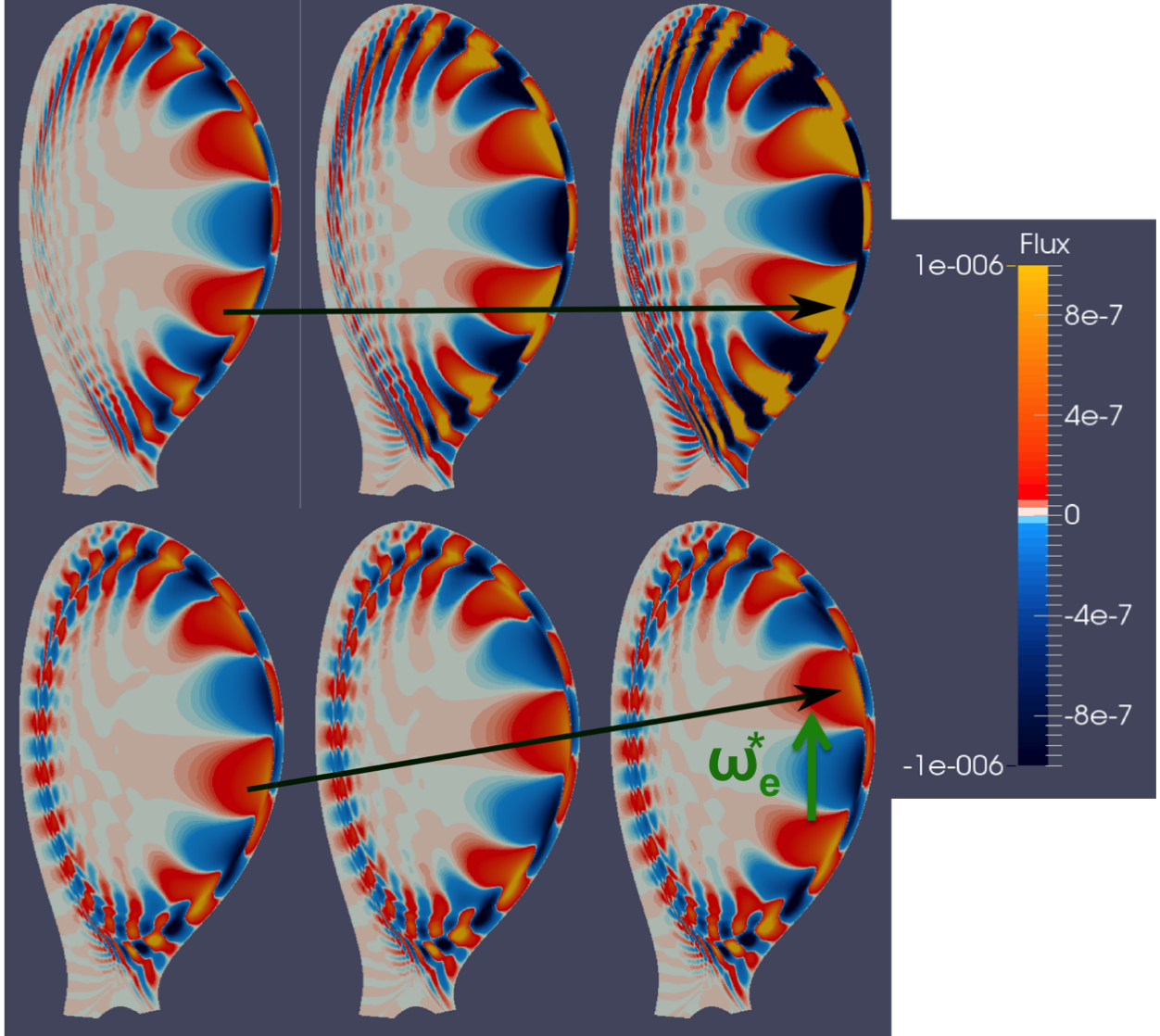


FIG. 2. Magnetic flux perturbation $n = 6$, same parameters as in Ref. [24] ($10 \mu s$ between images), (top) without diamagnetic effects and (bottom) with diamagnetic effects, $d_i = 1.7 \cdot 10^{-2}$. In the bottom the rotation is anticlockwise, i.e., in the electron diamagnetic or $\mathbf{E} \times \mathbf{B}$ direction.

146 other hand, if diamagnetic effects are taken into account the mode rotates in the electron
 147 diamagnetic direction with a velocity of several km/s . The $\mathbf{E} \times \mathbf{B}$ velocity is strongly
 148 reduced if diamagnetic effects are not taken into account since this velocity is proportional
 149 to d_i at the pedestal (see Eq. (11)).

150 We perform several computations varying the diamagnetic parameter, the resistivity and
 151 the parallel heat conductivity. The ballooning mode velocity rotation is plotted against
 152 the diamagnetic parameter in Fig. 3. In this figure we observe a linear scaling with the

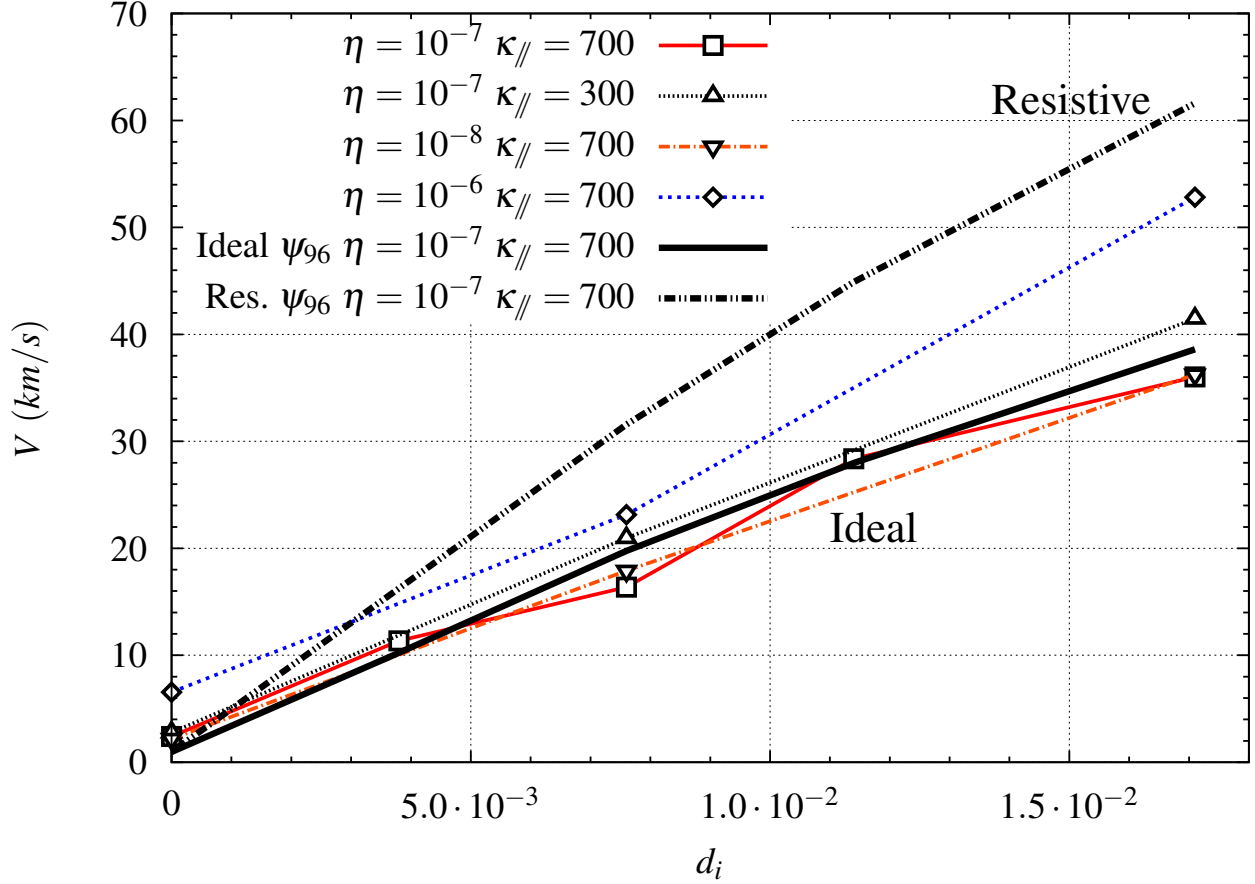


FIG. 3. Rotation velocity of the modes as a function of d_i and comparison with the expressions Eqs. (8) and (9) taken at Ψ_{96} (i.e. at the flux surface with $|\nabla P|_{max}$), κ_{\parallel} is the normalised parallel conductivity.

153 diamagnetic parameter d_i , in agreement with Eqs. (8) to (11).

154 In our simulations the $\mathbf{E} \times \mathbf{B}$ and the diamagnetic velocities dominate over the poloidally
 155 projected parallel velocity ($V_{\parallel} \cdot b_{\theta}$). For small resistivities, the numerical computations are
 156 close to the ideal formula Eq. (9) (thick black curve in Fig. 3). We observe that the ballooning
 157 mode velocity is always dominated by the $\mathbf{E} \times \mathbf{B}$ velocity, this mode always rotates in the
 158 electron diamagnetic direction. This can be explained as follows: at the pedestal, the ion
 159 diamagnetic and $\mathbf{E} \times \mathbf{B}$ velocities have approximately the same amplitude but opposite
 160 direction (see Eqs. (10) and (11)). For realistic cases (low resistivity) the system behaves
 161 close to the ideal limit. At this limit the ballooning mode rotates with half of the ion
 162 diamagnetic velocity (see Eq. (9)). As a consequence the $\mathbf{E} \times \mathbf{B}$ velocity is always larger
 163 and the ballooning mode rotates in the electron diamagnetic direction in the laboratory

164 reference frame.

165 In the present calculations we have not imposed a source of toroidal rotation. The par-
166 allel velocity comes from the Bohm boundary conditions that are imposed at the divertor.
167 Therefore the projected parallel velocity is small compared to the $\mathbf{E} \times \mathbf{B}$ and diamagnetic
168 velocities. In several devices as KSTAR the toroidal velocity can be very large. This ve-
169 locity must be taken into account in the calculation of the ELM precursors rotation in
170 the laboratory reference frame. Precursors rotating in the ion diamagnetic direction have
171 also been observed. This behaviour can be explained by a strong toroidal rotation that
172 counterbalances the $\mathbf{E} \times \mathbf{B}$ velocity.

173 III. NONLINEAR DYNAMICS OF ELM FILAMENTS

174 Experimentally the rotation of the modes is observed to decrease just before the ELM
175 crash [3, 6]. Also the observations show the rotation of the ELM filaments in the ion
176 diamagnetic direction [4, 6, 8]. This rotation is opposite to the one observed for the ELM
177 precursors.

178 With the JOREK code the nonlinear evolution of the ballooning modes is studied for a
179 case with $d_i = 7.6 \cdot 10^{-3}$. Near the ELM crash the density field can be observed on Fig. 4.
180 In this image, filaments of high density are expelled in the ion diamagnetic direction as
181 observed in the experiments.

182 The inversion of the rotation occurs at the nonlinear saturation of the instability. The
183 perturbed electric potential grows creating periodic vortices with alternating positive and
184 negative rotations. The strong correlation between the density and the electric potential can
185 be observed on Fig. 5(a). The $V_{\mathbf{E} \times \mathbf{B}}$ vortices are deformed, they are thinner in the radial
186 direction and elongated in the poloidal direction, following the magnetic field lines [26]. As
187 observed in Fig. 5(a) the density filament is convected by the $\mathbf{E} \times \mathbf{B}$ velocity vortex. Also
188 from the density ρ equation we can show that the density dynamic is governed by the $\mathbf{E} \times \mathbf{B}$
189 velocity term,

$$190 \quad \frac{\partial \rho}{\partial t} = \frac{1}{R} [\rho R^2, \Phi] + d_i \frac{\partial P}{\partial Z} + \text{Diff.} + \text{Source}, \quad (12)$$

191 with the Poisson bracket defined as: $[f, g] = \mathbf{e}_\phi \cdot (\nabla f \times \nabla g)$ (cylindrical coordinates). In this
192 equation the diamagnetic velocity (second term on the right hand side) does not act as an
193 advection term but only as a compression term. Therefore only the $\mathbf{E} \times \mathbf{B}$ velocity convects

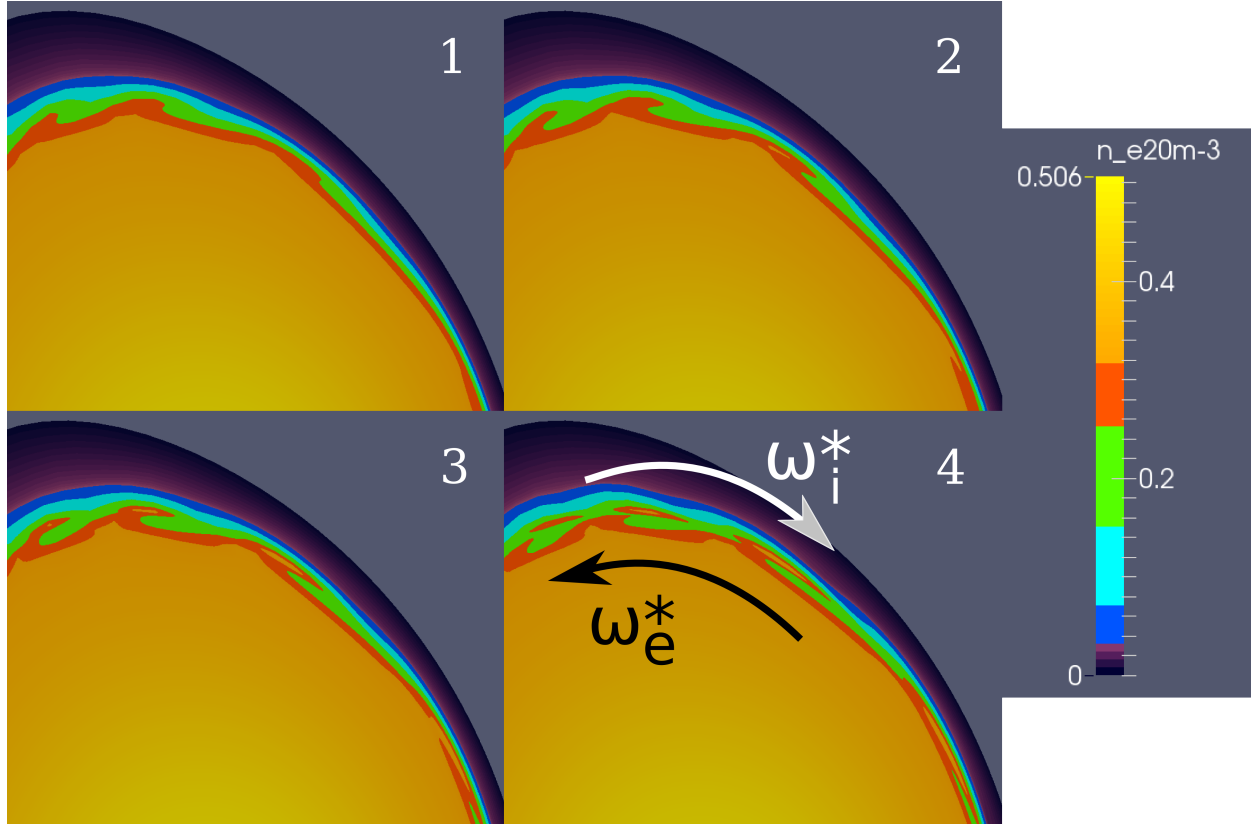


FIG. 4. Density filaments are expelled in ion diamagnetic direction, $d_i = 7.6 \cdot 10^{-3}$ ($5 \mu s$ between images).

194 the density filament (first term on the right hand side). The diamagnetic velocity does not
 195 convect directly the density but plays an important role in the nonlinear interactions. As we
 196 show later, the diamagnetic effects have a non-negligible influence on the $\mathbf{E} \times \mathbf{B}$ vorticity.

197 The profiles of the axisymmetric component of the $\mathbf{E} \times \mathbf{B}$ velocity are plotted on Fig. 6
 198 as a function of the normalised magnetic flux. From this figure we notice a strong velocity
 199 shear created during the ELM crash (see also Fig. 5(b)). At the same time as the filament
 200 is convected, a strong $\mathbf{E} \times \mathbf{B}$ shear appears. In the region where the mode perturbation is
 201 larger (around $\Psi_N = 0.96$) the velocity profile decreases and crosses the zero abscissa axis.
 202 This can explain why experimentally the ELM precursors decelerate approaching the crash.
 203 The shear increases further and the $\mathbf{E} \times \mathbf{B}$ velocity becomes negative. This effect makes
 204 the high density filament to cut from the main plasma, the filament is expelled.

205 Also in Ref. [12], without diamagnetic effects, a strong $\mathbf{E} \times \mathbf{B}$ shear was present in the
 206 nonlinear phase. The major difference with respect to the present computations is the initial

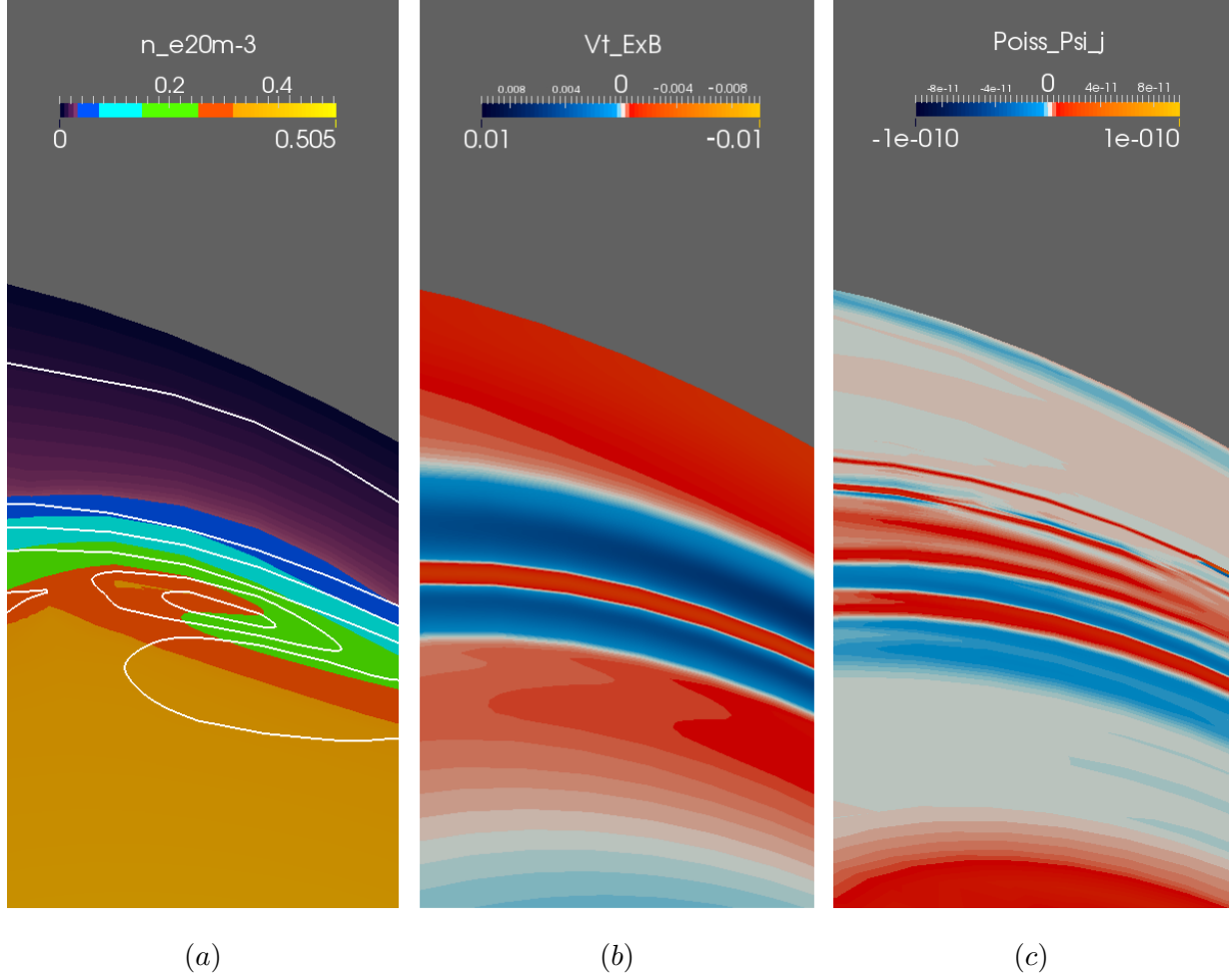


FIG. 5. (a) Density filament (colormap) and electric potential isocontours (white lines), (b) normalised axisymmetric $\mathbf{E} \times \mathbf{B}$ velocity and (c) Maxwell stress term $R^{-1} [\Psi, j]$. All these quantities are taken at the same instant, during the ELM crash ($t = 1273 \mu s$ in Figs. 6 and 7).

207 $V_{\mathbf{E} \times \mathbf{B}}$ profile, the profile was close to zero in the cited reference.

208 The different terms of the $\mathbf{E} \times \mathbf{B}$ vorticity w_E equation, implemented in the JOREK
 209 code, are plotted as a function of time in Fig. 7 (averaged on the closed flux surface region
 210 for $n = 0$). In weak form the vorticity equation yields

$$\begin{aligned}
 \delta_t w_E = & - \int \hat{\rho} \nabla u^* \cdot \nabla_{\perp} (\delta_t \Phi) dV = \int \left(- \frac{v_E^2}{2R} [u^*, \hat{\rho}] - R \hat{\rho} w_E [u^*, \Phi] + R [u^*, P] \right. \\
 & \left. - u^* \nabla \phi \cdot \nabla \times (R^2 \rho (\mathbf{v}_i^* \cdot \nabla) \mathbf{v}_E) - u^* \frac{1}{R} [\Psi, j] + u^* \frac{F_0}{R^2} \partial_{\phi} j + u^* \nabla \phi \cdot \nabla \times (R^2 \mu \nabla^2 \mathbf{v}_E) \right) dV,
 \end{aligned}
 \tag{13}$$

211 with u^* a test function, ϕ the toroidal direction, μ the dynamic viscosity and $\hat{\rho} = R^2 \rho$. For

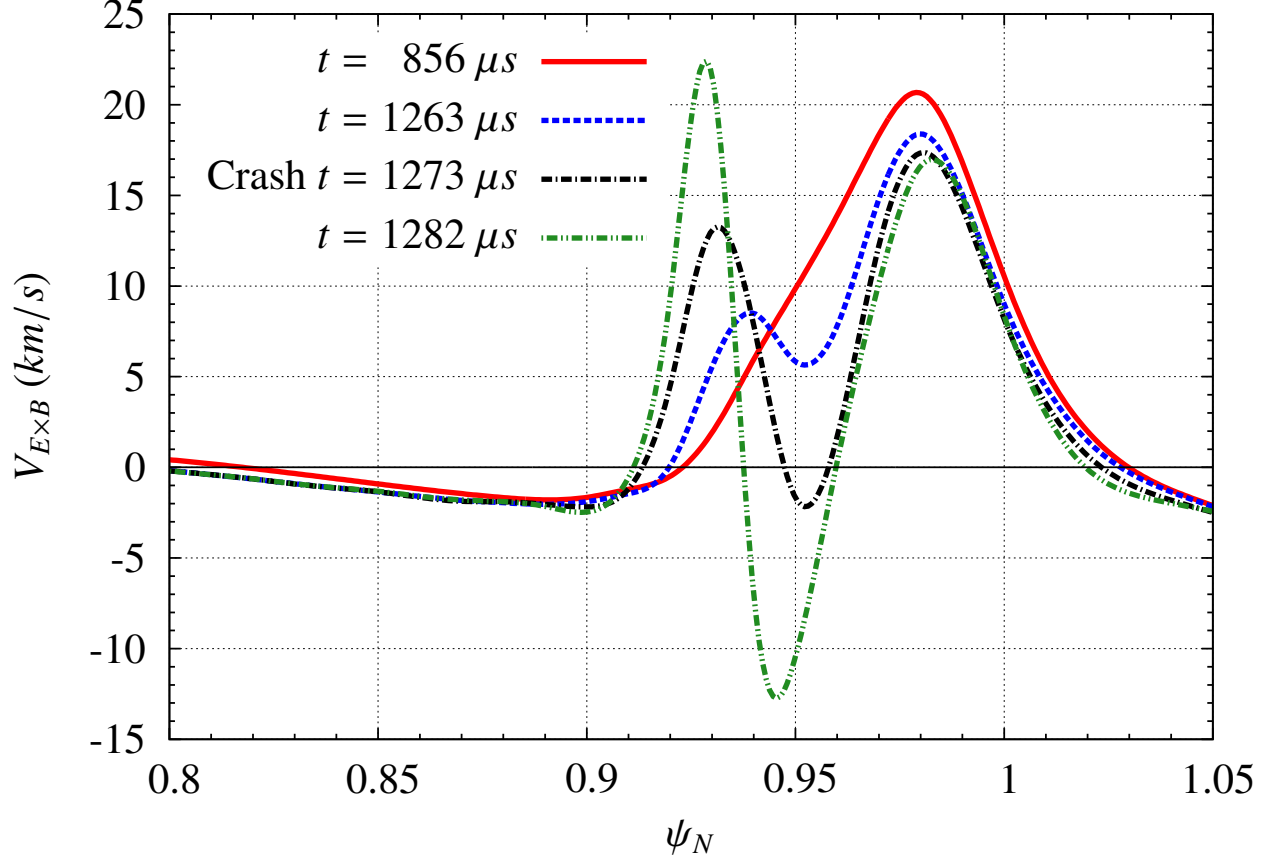


FIG. 6. Axisymmetric ($n = 0$) $\mathbf{E} \times \mathbf{B}$ velocity profiles during an ELM crash (averaged in the region between the low field side and the vertical direction $\theta = [0, \pi/2]$).

212 more details we refer to [12, 22, 23, 25].

213 In Fig. 7 the equilibrium noted Eq is the static equilibrium (pressure $R[u^*, P]$ plus
 214 Maxwell stress tensor, $R^{-1}[\Psi, j]$ term). Also axisymmetric equilibrium flows [27] generate
 215 viscous dissipation. We can observe that in the linear phase the static equilibrium Eq and
 216 viscosity terms balance, there is no vorticity generation. At $t = 1.24$ ms, the diamagnetic
 217 term $-\nabla\phi \cdot \nabla \times (R^2 \rho(\mathbf{v}_i^* \cdot \nabla) \mathbf{v}_E)$ (Dia) grows but is balanced by the equilibrium and viscosity
 218 terms. However a small growth of vorticity w_E is observed. Then at $t = 1.273$ ms (same
 219 time as in Fig. 5) the ELM crash occurs. The term $\delta_t w_E$ becomes large, strong vorticity is
 220 created. This vorticity is generated nonlinearly by the unbalance between the terms in the
 221 vorticity equation. The terms dominating the w_E dynamics are the Maxwell stress tensor
 222 $R^{-1}[\Psi, j]$ [12] (see also Fig. 5(c)) and the Dia term. On the other hand the pressure term
 223 $R[u^*, P]$ is large but does not behave with the same dynamic as the $\delta_t w_E$ term.

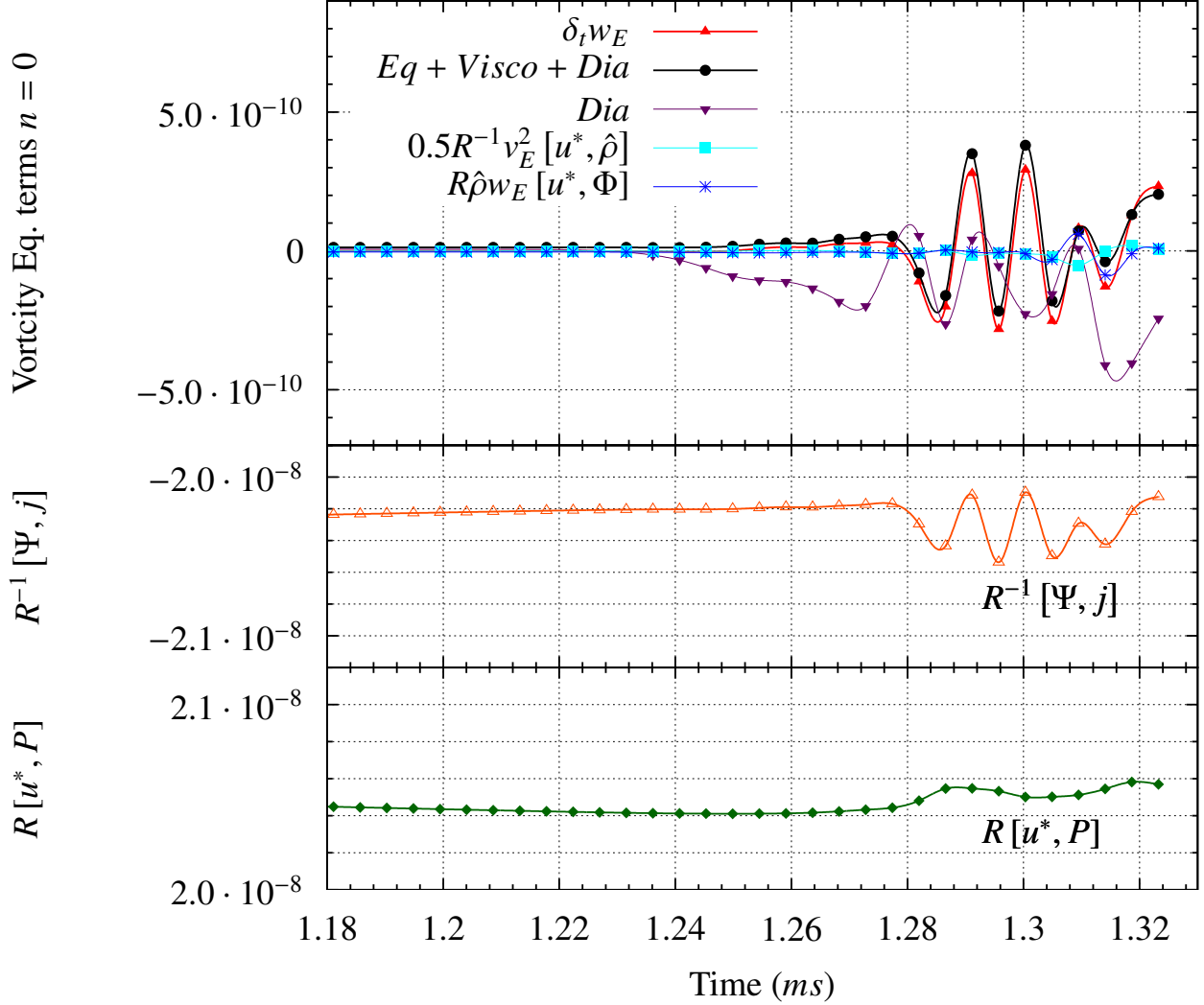


FIG. 7. Axisymmetric (toroidal mode number $n = 0$) $\mathbf{E} \times \mathbf{B}$ vorticity equation terms (see Eq. (13)) as a function of time.

224 IV. CONCLUSION

225 In the linear phase the analytical ideal ballooning calculations and the JOREK simu-
 226 lations are in good agreement. They explain why experimentally the ELM precursors are
 227 mainly observed rotating in the electron diamagnetic direction.

228 Near the ELM crash we find a strong nonlinear generation of axisymmetric $\mathbf{E} \times \mathbf{B}$ velocity
 229 shear. This shear makes the density filaments to be expelled outside the main plasma. Also
 230 the filaments rotation is opposite to the ELM precursors rotation, i.e., in the ion diamagnetic
 231 direction, as observed experimentally. The Maxwell stress and diamagnetic terms govern

232 the vorticity generation at the nonlinear phase.

233 The ELM crash is a strong nonlinear event (see e.g. [28]). In this letter we focus on
234 the early stages of the ELM crash. We observe that the strong $\mathbf{E} \times \mathbf{B}$ shear plays an
235 important role in the ELM filament detachment. Another important transport channel is
236 parallel conduction [29]. Reconnection [30] is also observed at the early stages of the ELM
237 crash and certainly plays an important role on the density and energy transport towards the
238 plasma-facing components, in particular towards the tokamak divertor.

239 As a perspective for this work we can mention the study of the toroidal velocity profile.
240 In this work we have not imposed a toroidal velocity source but it would certainly be an im-
241 portant element to take into account in future simulations of ELM precursors. The toroidal
242 velocity profile not only influences the precursors rotation but also the linear ballooning
243 dispersion relation if a shear exists (see e.g. [31]).

244 ACKNOWLEDGMENTS

245 We thank C. Norscini, P. Tamain and N. Fedorczak for interesting discussions on this work. This
246 project has been carried out within the framework of the EUROfusion Consortium and has received
247 funding from the Euratom research and training programme 2014-2018 under grant agreement
248 No. 633053. This work has benefited from financial support from the National French Research
249 Program (ANR): ANEMOS (2011). A part of this work was carried out using the CCRT-CURIE
250 supercomputer within project GENCI (gen2197) and PRACE (ra1904) and the HELIOS super-
251 computer system (IFERC-CSC). The views and opinions expressed herein do not necessarily reflect
252 those of the European Commission or the ITER Organization.

-
- 253 [1] A. Leonard, *Physics of Plasmas* **21**, 090501 (2014).
254 [2] G. Huijsmans, C. Chang, N. Ferraro, L. Sugiyama, F. Waelbroeck, X. Xu, A. Loarte, and
255 S. Futatani, *Physics of Plasmas* **22**, 021805 (2015).
256 [3] G. Yun, W. Lee, M. Choi, J. Lee, H. Park, B. Tobias, C. Domier, N. Luhmann Jr, A. Donn e,
257 J. Lee, *et al.*, *Physical Review Letters* **107**, 045004 (2011).
258 [4] J. Boom, I. Classen, P. De Vries, T. Eich, E. Wolfrum, W. Suttrop, R. Wenninger, A. Donn e,

- 259 B. Tobias, C. Domier, *et al.*, Nuclear Fusion **51**, 103039 (2011).
- 260 [5] I. Classen, J. Boom, A. Bogomolov, E. Wolfrum, M. Maraschek, W. Suttrop, P. de Vries,
261 A. Donn e, B. Tobias, C. Domier, *et al.*, Nuclear Fusion **53**, 073005 (2013).
- 262 [6] Y. Sechrest, T. Munsat, D. Battaglia, and S. Zweben, Nuclear Fusion **52**, 123009 (2012).
- 263 [7] R. Wenninger, H. Reimerdes, O. Sauter, and H. Zohm, Nuclear Fusion **53**, 113004 (2013).
- 264 [8] A. Kirk, D. Dunai, M. Dunne, G. Huijsmans, S. Pamela, M. B coulet, J. Harrison,
265 J. Hillesheim, C. Roach, and S. Saarelma, Nuclear Fusion **54**, 114012 (2014).
- 266 [9] M. Rack, B. Sieglin, J. Pearson, T. Eich, Y. Liang, P. Denner, A. Wingen, L. Zeng, I. Balboa,
267 S. Jachmich, *et al.*, Nuclear fusion **54**, 064012 (2014).
- 268 [10] P. Manz, J. Boom, E. Wolfrum, G. Birkenmeier, I. Classen, N. Luhmann Jr, U. Stroth, *et al.*,
269 Plasma Physics and Controlled Fusion **56**, 035010 (2014).
- 270 [11] P. Snyder, H. Wilson, J. Ferron, L. Lao, A. Leonard, T. Osborne, A. Turnbull, D. Mossessian,
271 M. Murakami, and X. Xu, Physics of Plasmas **9**, 2037 (2002).
- 272 [12] G. Huysmans and O. Czarny, Nuclear Fusion **47**, 659 (2007).
- 273 [13] O. Czarny and G. Huysmans, Journal of Computational Physics **227**, 7423 (2008).
- 274 [14] D. Schnack, D. Barnes, D. Brennan, C. Hegna, E. Held, C. Kim, S. Kruger, A. Pankin, and
275 C. Sovinec, Physics of Plasmas **13**, 058103 (2006).
- 276 [15] J. Connor, R. Hastie, and J. Taylor, in *Proceedings of the Royal Society of London A: Math-*
277 *ematical, Physical and Engineering Sciences*, Vol. 365 (The Royal Society, 1979) pp. 1–17.
- 278 [16] P. Diamond, P. Similon, T. Hender, and B. Carreras, Physics of Fluids **28**, 1116 (1985).
- 279 [17] K. Roberts and J. Taylor, Physical Review Letters **8**, 197 (1962).
- 280 [18] W. Tang, R. L. Dewar, and J. Manickam, Nuclear Fusion **22**, 1079 (1982).
- 281 [19] G. Huysmans, S. Sharapov, A. Mikhailovskii, and W. Kerner, Physics of Plasmas **8**, 4292
282 (2001).
- 283 [20] G. Huysmans, Plasma Physics and Controlled Fusion **47**, B165 (2005).
- 284 [21] E. Viezzer, T. P tterich, G. Conway, R. Dux, T. Happel, J. Fuchs, R. McDermott, F. Ryter,
285 B. Sieglin, W. Suttrop, *et al.*, Nuclear Fusion **53**, 053005 (2013).
- 286 [22] S. Pamela, G. Huysmans, M. Beurskens, S. Devaux, T. Eich, S. Benkadda, *et al.*, Plasma
287 Physics and Controlled Fusion **53**, 054014 (2011).
- 288 [23] F. Orain, M. B coulet, G. Dif-Pradalier, G. Huijsmans, S. Pamela, E. Nardon, C. Passeron,
289 G. Latu, V. Grandgirard, A. Fil, *et al.*, Physics of Plasmas **20**, 102510 (2013).

- 290 [24] M. Bécoulet, F. Orain, G. Huijsmans, S. Pamela, P. Cahyna, M. Hoelzl, X. Garbet, E. Franck,
291 E. Sonnendrücker, G. Dif-Pradalier, *et al.*, Physical Review Letters **113**, 115001 (2014).
- 292 [25] A. Fil, E. Nardon, M. Hoelzl, G. T. A. Huijsmans, F. Orain, M. Becoulet, P. Beyer, G. Dif-
293 Pradalier, R. Guirlet, H. R. Koslowski, M. Lehnen, J. Morales, S. Pamela, C. Passeron,
294 C. Reux, F. Saint-Laurent, and J. Contributors, Physics of Plasmas **22** (2015).
- 295 [26] N. Fedorczak, P. Diamond, G. Tynan, and P. Manz, Nuclear Fusion **52**, 103013 (2012).
- 296 [27] S. Pamela, G. Huysmans, and S. Benkadda, Plasma Physics and Controlled Fusion **52**, 075006
297 (2010).
- 298 [28] H. Wilson and S. Cowley, Physical Review Letters **92**, 175006 (2004).
- 299 [29] T. Rhee, S. S. Kim, H. Jhang, G. Y. Park, and R. Singh, Nuclear Fusion **55**, 032004 (2015).
- 300 [30] R. Fitzpatrick, Physics of Plasmas **1**, 3308 (1994).
- 301 [31] H. Wilson, P. Buxton, and J. Connor, *Rotation and momentum transport in magnetized*
302 *plasmas (reviews of the theory of magnetized plasmas)*, edited by P. Diamond, X. Garbet,
303 P. Ghendrih, and Y. Sarazin (World Scientific Publishing Co, 2015) Chap. 5.